# Super-Resolution Photoacoustic Imaging by Modulation of the Point Spread Function

Reza Rahpeima[1], Chi-Wei Huang[1], Jian-yu Lu[2], Pai-Chi Li[1,*]

[1] College of Electrical Engineering and Computer Science, National Taiwan University, Taipei, Taiwan.

[2] Department of Bioengineering, College of Engineering, The University of Toledo, Toledo, Ohio, USA.

[*] Corresponding author, Email: paichi@ntu.edu.tw

Tel./Fax: +886-2-33663551/+886-2-83691354

## Abstract

Photoacoustic imaging (PAI) offers high optical contrast and ultrasound-level spatial resolution at depth, but the method is fundamentally constrained by acoustic diffraction. Here we report how modulating the point spread function (PSF) can achieve super-resolution PAI, implemented via localized amplitude modulation with a physical modulator. This study is the first to investigate this approach in the context of PAI. Subtracting the signals acquired with and without the modulator makes it possible to isolate components with high spatial frequencies corresponding to fine structural features, which are used to reconstruct images with spatial features smaller than the conventional diffraction limit. Comprehensive finite-element method (FEM) simulations incorporating ray optics, heat transfer, solid mechanics, and pressure acoustics were performed alongside controlled experiments. The method was validated using a raster scanning setup with a single-element transducer applied to two object configurations: one with three parallel strands and the other with four strands in an X-shaped arrangement. The results demonstrate that our novel approach achieves a sixfold improvement in spatial resolution; for example, using a transducer with a center frequency of 10 MHz allowed features separated by as little as 0.1 mm to be clearly resolved, compared with the system's native resolution of approximately 0.6 mm. This work has established PSF modulation as a robust and generalizable strategy, laying the foundation for future advancements in achieving super-resolution PAI without the need for advanced transducer systems with large apertures or tight focusing, exogenous contrast agents, or motion-dependent techniques.

**Keywords** photoacoustic imaging, super resolution, PSF modulation, photoacoustic microscopy, biomedical imaging.

## 1. Introduction

Photoacoustic imaging (PAI) is an emerging biomedical imaging modality in which the high spatial resolution of ultrasound (US) imaging is cooperatively combined with the excellent contrast and molecular specificity of optical imaging [1]. In PAI, pulsed laser irradiation induces localized thermoelastic expansion in biological tissues, generating US waves that are subsequently detected to reconstruct images [1].

Despite its advantages, the spatial resolution of PAI—particularly at greater depths—is fundamentally limited by both optical scattering and the acoustic diffraction limit. The scattering that occurs as light propagates within tissue reduces the optical fluence and blurs the spatial distribution of the absorbed energy, making it impossible to maintain strong optical focusing beyond shallow depths [2]. PAI operates in acoustic-resolution mode in this deep-tissue regime, where spatial resolution is constrained by the acoustic diffraction limit. The use of higher US frequencies improves the spatial resolution but increases the



Preprint not peer reviewed

This preprint research paper has not been peer reviewed. Electronic copy available at: https://ssrn.com/abstract=5749641

attenuation, and hence restricts the imaging depth. The resulting rapid degradation in resolution with depth poses challenges for high-resolution clinical and preclinical imaging [3].

Numerous approaches have been developed to overcome the diffraction-limited resolution of PAI, prompting investigations into super-resolution techniques to enhance its spatial resolution. These methods seek to surpass the conventional resolution limits governed by the acoustic wavelength or optical diffraction. The super-resolution techniques that have demonstrated promise in PAI include localization-based methods, fluctuation analysis, structured illumination, wavefront shaping, and advanced beamforming techniques [4].

Localization-based PAI leverages the sparse distribution of absorbers and tracks their positions over multiple frames to reconstruct high-resolution images. In 2018, Luís Dean-Ben and Razansky introduced the novel LOT (localization optoacoustic tomography) concept that employs the rapid sequential acquisition of three-dimensional (3D) optoacoustic images from flowing absorbing particles [5]. Also, microbubble-assisted localization has made it possible to improve the lateral resolution well beyond the acoustic diffraction limit [6]. However, the requirement for isolated absorbers and long acquisition times limits the practicality of these localization-based PAI methods.

Fluctuation-based techniques such as SOFI (super-resolution optical fluctuation imaging) have been adapted to PAI by analyzing the temporal fluctuations of signals from dynamic absorbers such as red blood cells or flowing contrast agents [7]. These approaches can improve the resolution by the application of statistical postprocessing, although their reliance on motion or dynamic absorbers represents a key limitation [8].

SI-PAM (structured illumination photoacoustic microscopy) employs patterned light excitation to encode high spatial frequencies into the detectable signal. This technique utilizes computational reconstruction to increase the resolution, but the occurrence of light scattering typically restricts it to shallow imaging depths [9, 10].

Wavefront shaping is a promising technique for improving the spatial resolution of PAI by focusing light deep into scattering tissue through phase modulation of the incident wavefront. This method improves signal localization using PA feedback. However, its application in real-time or in-vivo settings is restricted by its slow optimization speed, sensitivity to motion, and the need for stable measurement conditions [11, 12].

Beamforming and signal processing techniques have also been employed to achieve super-resolution PAI. Methods such as adaptive beamforming (e.g., minimum variance) and synthetic aperture reconstruction improve the resolution beyond the acoustic diffraction limit by improving the spatial coherence and thereby effectively expanding the aperture. These approaches refine the point spread function (PSF) and suppress artifacts, enabling clearer visualization of fine structures at greater depths [13, 14].

Modulation of the PSF has recently emerged as a promising strategy for surpassing the diffraction limit and enabling super-resolution imaging in US systems [15, 16]. This can be achieved through amplitude or phase modulation, where the PSF is altered to increase the spatial resolution beyond conventional limits. In 2023, Lu increased the spatial frequency content of the PSF via amplitude and phase control by using small modulators and focused shear waves [16]. Both simulations and US experiments showed that the resolution could be improved 7.26-fold relative to the conventional diffraction limit of ~3.63 mm, to image features as small as ~0.5 mm [16, 17]. In another study the same author achieved super-resolution by modulating the PSF of the receiver to measure spatially varying acoustic fields, which also improved the image resolution beyond the diffraction limit [18].



Preprint not peer reviewed

This preprint research paper has not been peer reviewed. Electronic copy available at: https://ssrn.com/abstract=5749641

Motivated by the demonstrated success of PSF modulation in overcoming the diffraction limit in US imaging, in the present study we aimed to characterize its potential in PAI, which shares the same acoustic detection principles. PSF modulation offers a promising approach for achieving super-resolution PAI without relying on high-frequency transducers or contrast agents, yet its application in PAI has remained largely unexplored. This study investigated the feasibility and effectiveness of applying PSF modulation to improve the spatial resolution of PAI.

Target objects with different configurations were considered, and detailed physics-based finite-element method (FEM) simulations of PAI were performed. FEM solvers are highly suitable for complex multiphysics problems in which distinct physical phenomena such as acoustics and heat transfer must be accurately coupled and simulated [19-25]. Our simulations incorporated ray optics, heat transfer, solid mechanics, and pressure acoustics to realistically model all of the involved physical processes. Complementary experiments were also performed under similar conditions to validate the simulation results. This study aimed to demonstrate that the intrinsic spatial resolution of the imaging system—which is normally constrained by the diffraction limit—can be significantly improved through the application of PSF modulation, yielding super-resolved images. Several challenges were addressed in this study, including limitations of the signal-to-noise ratio (SNR), precise control of modulation mechanisms, and integration with imaging systems, and the effects of key parameters were thoroughly investigated.

This paper is structured as follows: Section 2 outlines the methodology used, including the modulation principles, imaging strategy, simulation procedure, and experimental setup; Section 3 reports both simulation and experimental results; Section 4 discusses these results in detail; and conclusions are drawn in Section 5.

## 2. Materials & methods

This section describes the methodology used to investigate the application of PSF modulation for achieving super-resolution PAI. We begin by outlining the principles and implementation of the PSF modulation technique.

### 2.1. PSF modulation

PSF modulation can be implemented through amplitude modulation, phase modulation, or a combination of both methods. Amplitude modulation of the PSF involves selectively reducing the amplitude of the imaging wave within a localized region near the focal point, which is typically achieved using a small modulating device such as an absorber or scatterer. The modulation function defines a central area where the PSF amplitude is suppressed to zero, while the surrounding region remains unchanged, thereby creating a localized minimum in the spatial profile. Subtracting the PSF acquired with the modulator from the original (unmodulated) PSF introduces abrupt spatial variations that translate into increased high-frequency components in the Fourier domain. These components correspond to fine structural details that are normally lost due to diffraction-related blurring. By isolating these components, the method enables the reconstruction of images with spatial features smaller than the conventional diffraction limit.

On the other hand, phase modulation of the PSF is achieved by generating shear waves in the medium, which induce localized phase shifts in the imaging wave. This controlled modulation alters the interference patterns of the PSF to redistribute energy to higher spatial frequencies. Subtracting the modulated PSF from the original reveals fine structural details, again enabling super-resolution image reconstruction beyond the diffraction limit.



Preprint not peer reviewed

This preprint research paper has not been peer reviewed. Electronic copy available at: https://ssrn.com/abstract=5749641

A comprehensive mathematical explanation of both PSF modulation methods, along with illustrative figures, is available in references [17, 26]. The present study applied the amplitude modulation technique to achieve super-resolution PAI.

### 2.2. Imaging strategy

A raster scanning-based imaging system was combined with a single-element transducer. Signals corresponding to each image pixel were acquired by moving the transducer in a stepwise manner across a defined spatial grid. A small physical obstacle, referred to as the modulator, was placed at the focal point of the transducer to locally block or alter wave propagation. Signals were acquired for each pixel both with and without the modulator in place.

The amplitude modulation analysis fundamentally involved subtracting the signal amplitudes acquired with and without the modulator at each scanning position and at a selected depth. However, experimental challenges meant that additional signal processing procedures needed to be implemented to correct for several factors. For example, temporal fluctuations in the laser power resulting from the long acquisition time associated with mechanical raster scanning were addressed by scaling the modulated signals to match the total energy of the unmodulated signals. This compensated for the gradual reduction in the laser power during time. Also, temporal alignment of the signals was performed by applying a time shift to synchronize the first peaks of the modulated and unmodulated signals, which corrected for delays introduced by the presence of the modulator. After image acquisition, a brief image processing step was applied to reduce pixelation and produce smoother, more visually appealing images. Specifically, bicubic interpolation was used to upscale the images by a specific factor, increasing the number of pixels and improving the visual clarity. The overall research workflow is illustrated as a flowchart in Fig. 1.

To obtain comprehensive results, we performed detailed, 3D physics-based simulations of the entire PAI process using the FEM. Simulations and experiments were conducted in parallel to ensure consistency between the computational predictions and real-world observations.



Preprint not peer reviewed

This preprint research paper has not been peer reviewed. Electronic copy available at: https://ssrn.com/abstract=5749641

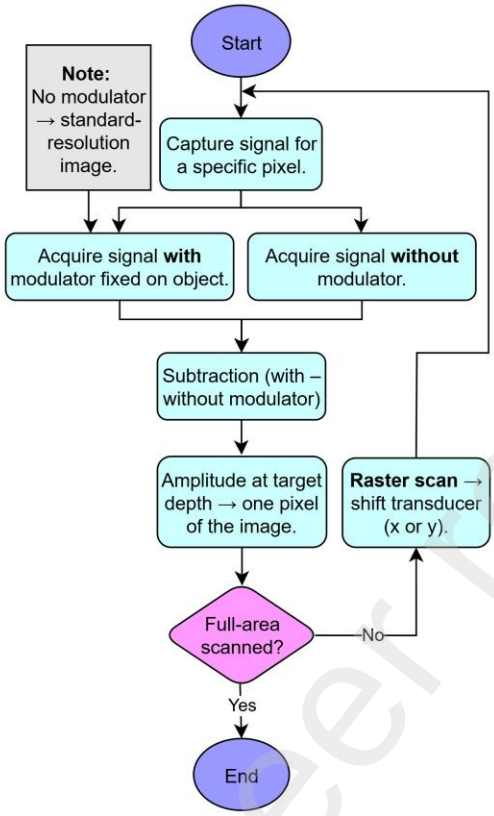


**Fig. 1** Flowchart of the super-resolution PAI procedure.

### 2.3. Simulations and experimental setup

Simulations of the PAI phenomenon incorporating four distinct physics processes—ray optics, heat transfer, solid mechanics, and pressure acoustics—were performed using COMSOL Multiphysics software. Laser irradiation was first simulated, followed by the absorption of laser energy by the object and the subsequent temperature increases. The resulting thermoelastic expansion led to the generation of pressure stresses. These processes were modeled by coupling the three physics processes of ray optics, heat transfer, and solid mechanics. The resulting pressure was then used as the initial condition in the pressure acoustics module that simulated the propagation of pressure waves. These waves were subsequently detected by the transducer, and signal processing and image reconstruction were applied to the detected signals. This simulation platform, including the governing equations, simulation parameters, boundary conditions, and method used for mesh optimization, are comprehensively explained here [20].

As mentioned above, a raster scanning-based PAI system was employed. A scanning step size of 0.1 mm was chosen to ensure fine spatial sampling across the imaging domain. The scanning process was carried out using a three-axis mechanical translation stage. The imaged objects consisted of closely spaced black hair strands, each approximately 0.1 mm in diameter, placed on top of a thin microscope slide and submerged at the bottom of a water-filled container to facilitate the propagation of acoustic waves. The physical modulator used to apply amplitude modulation to the PSF was constructed from two crossed plastic wires, each 0.1 mm in diameter and positioned at the transducer's focal point, directly above the imaging object. The modulator was held in place using a custom-designed 3D-printed holder precisely aligned with the transducer and the rest of the experimental setup.



Preprint not peer reviewed

This preprint research paper has not been peer reviewed. Electronic copy available at: https://ssrn.com/abstract=5749641

Illumination was provided by a pulsed laser operating at 580 nm (red light), with a pulse width of 10 ns and a repetition rate of 20 Hz. The circular collimated laser beam with a fixed diameter of 3 mm entered from the bottom of the water container. A focused single-element transducer located at the top of the container was used to detect the generated PA waves. The transducer had a focal length of 3 cm, an aperture size of 1 cm, and a center frequency of 10 MHz. These transducer specifications would produce a system with a theoretical diffraction-limited lateral resolution without PSF modulation of approximately 0.6 mm, as estimated using the following classical formula [27]:

$$\text{Lateral Resolution} \approx 1.22 \cdot \frac{\lambda \cdot F}{D} \tag{1}$$

where $\lambda$ is the acoustic wavelength, $F$ is the focal length of transducer, and $D$ is the aperture diameter. The simulation geometry that precisely replicated the experimental setup described above is shown in Fig. 2(a). The modulator and its 3D-printed holder are shown separately in Fig. 2(b), a photograph of the complete experimental setup is presented in Fig. 2(c), and a schematic illustration of the setup is provided in Fig. 2(d).

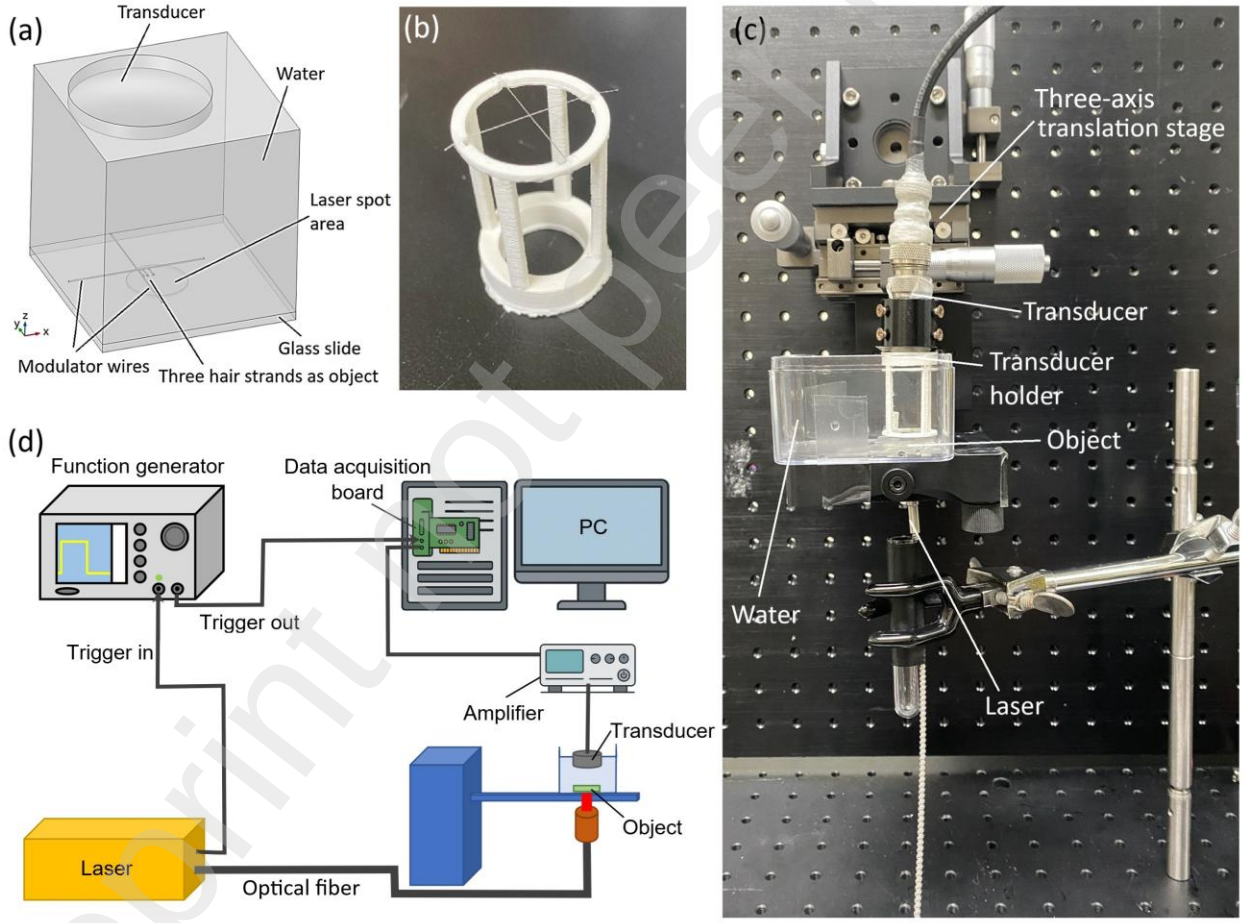


**Fig. 2** (a) Simulation geometry, (b) modulator, (c) experimental setup, and (d) schematic of the PAI system.

Two distinct objects were considered in this study. The first object consisted of three parallel hair strands placed in close proximity, with spacings of 0.1 mm and 0.2 mm in the simulations, and of 0.1–0.3 mm in the experiments. The latter range was broader since minor measurement uncertainties in the experimental setup made it difficult to precisely control the strand spacing. The raster scanning domain was set to 10 and



Preprint not peer reviewed

This preprint research paper has not been peer reviewed. Electronic copy available at: https://ssrn.com/abstract=5749641

4 steps in the *x*- and *y*-directions, respectively, in the simulations, and 20 and 4 steps in the experiments. Each step measured 0.1 mm in both configurations. The second object comprised four hair strands in an X-shaped arrangement, spaced by 0.1 mm in the simulations and by 0.1–0.3 mm in the experiments (again larger due to measurement uncertainties). Both the simulations and experiments used a raster scanning grid of 20 × 20 steps with a step size of 0.1 mm. The objects used in the simulations and experiments along with their respective raster scanning domains and the laser spot areas are illustrated in Fig. 3: Fig. 3(a) and 3(b) show the first configuration and Fig. 3(c) and 3(d) show the second configuration.

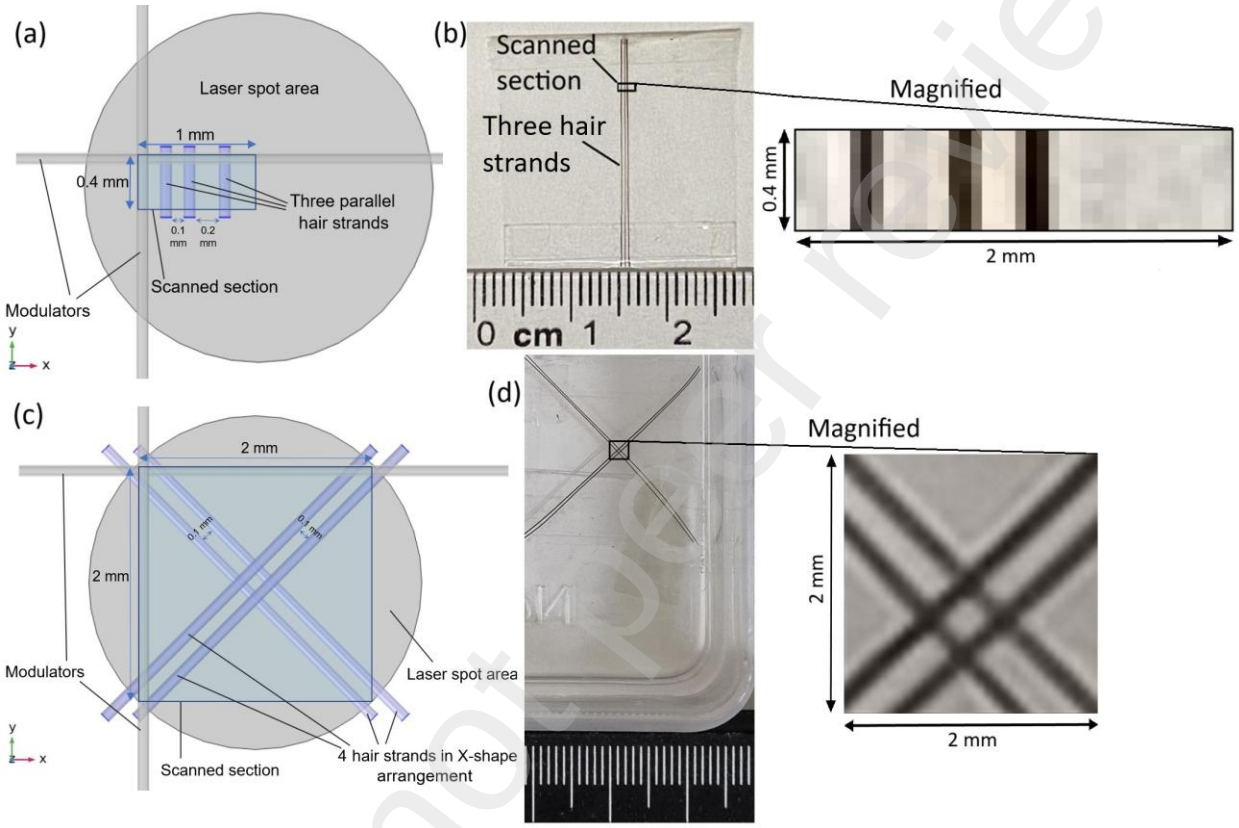


**Fig. 3** Configurations of the three parallel hair strands in the simulations (a) and experiments (b), and of the X-shaped arrangement of four hair strands in the simulations (c) and experiments (d).

## 3. Results

The results obtained when using three parallel hair strands or an X-shaped arrangement of four hair strands as the imaging object are reported below. Also, an image postprocessing step for visualization improvement was applied to enable clearer comparisons and provide a better understanding of the effects of PSF modulation on the reconstructed PA images.

### 3.1. Parallel strands

Fig. 4 shows the results corresponding to each intermediate physical process for one of the simulations representing a single pixel of the image when the modulator was not present. The initial ray configuration at the laser spot area is shown in Fig. 4(a). A cylindrical region with a uniform angular and radial grid is considered, resulting in the energy intensity peaking at the center and gradually decreasing toward the edges of the spot. The laser was operated with a 10-ns pulse width. The hair strands absorbed the laser energy and



This preprint research paper has not been peer reviewed. Electronic copy available at: https://ssrn.com/abstract=5749641

increased in temperature, with the resulting temperature distribution after 10 ns shown in Fig. 4(b). This temperature rise led to thermoelastic expansion of the strands, whose displacements and pressure distributions after one pulse duration are illustrated in Fig. 4(c) and 4(d), respectively. The pressure generated at the hair strands then propagated outward to be detected by the transducer located at the top of the container. The acoustic pressure distribution after 12 μs of propagation is shown in Fig. 4(e). This simulation process was repeated for each image pixel using the raster scanning approach both with and without the modulator.

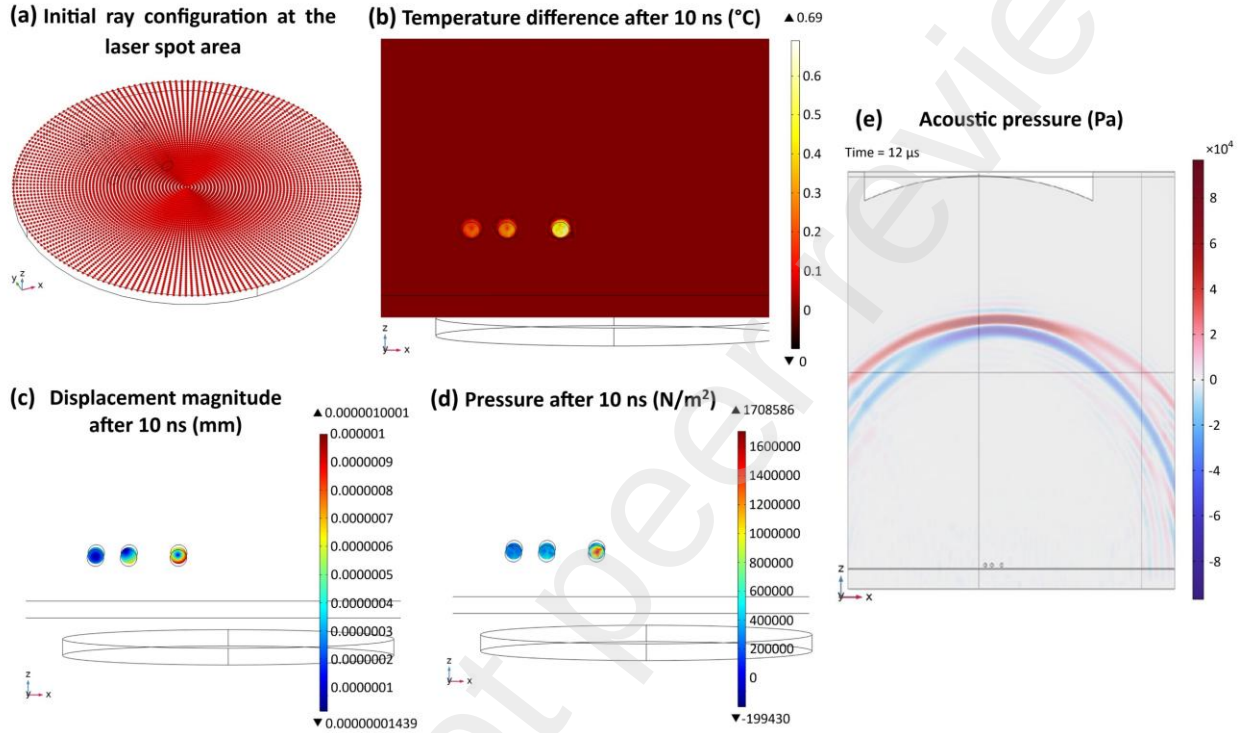


**Fig. 4** (a) Initial ray configuration in the laser illumination area. (b) Temperature increase after a single laser pulse. (c) Displacements generated by a single laser pulse. (d) Pressures generated by a single laser pulse. (e) Acoustic pressure field at 12 μs after the pressure generation.

Fig. 5 shows the final images after performing amplitude modulation as described in Section 2.2 for the simulations and experiments at a specific depth corresponding to the surface of the object obtained after collecting all of the signals for each pixel both with and without the modulator. The simulation object and the experimental ground-truth object are shown in Fig. 5(a) and 5(g), respectively. The results for the baseline simulation and experiment are illustrated in Fig. 5(b) and 5(h), respectively, without the modulator present, and in Fig. 5(d) and 5(j) with the modulator present. The resulting super-resolution reconstructions are presented in Fig. 5(c) for the simulation and Fig. 5(i) for the experiment. It can be seen that the resulting images appear pixelated and lacking smoothness due to the small number of pixels resulting from restricted raster scanning steps.

To address this issue and improve the visual quality of the reconstructed images, bicubic interpolation was applied as a postprocessing step to increase the pixel density and reduce pixelation artifacts. Specifically, an interpolation factor of 2 was used in both the lateral ($x$) and elevational ($y$) directions. This effectively quadrupled the pixels in the two-dimensional image domain, resulting in a smoother and more-continuous intensity distribution. Compared with nearest-neighbor and bilinear interpolation methods,



Preprint not peer reviewed

This preprint research paper has not been peer reviewed. Electronic copy available at: https://ssrn.com/abstract=5749641

bicubic interpolation provides smoother images with better-preserved gradients, making it well suited for visual improvement without introducing significant artifacts.

To facilitate visual comparisons, the without-modulator (baseline) images and the super-resolution images obtained after bicubic interpolation are displayed alongside the original reconstructed results in Fig. 5. Fig. 5(e) and 5(f) present the simulation results after bicubic interpolation, while Fig. 5(k) and 5(l) show the corresponding experimental results after bicubic interpolation.

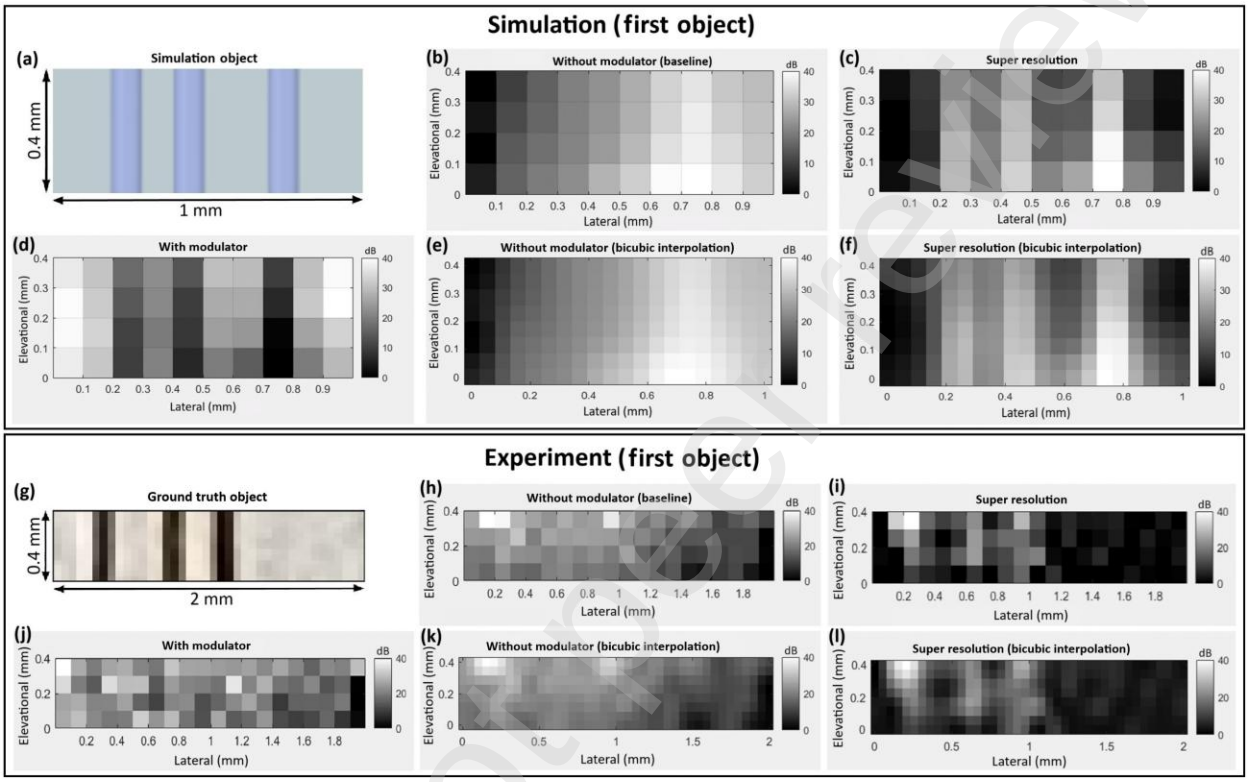


**Fig. 5** Reconstructed PA images at a fixed depth corresponding to the surface of the first object comprising three parallel hair strands. (a–f) Simulation: (a) simulation object, (b) without modulator, (c) super resolution, (d) with modulator, (e) without modulator after bicubic interpolation, and (f) super resolution after bicubic interpolation. (g–l) Experiment: (g) ground-truth experimental object, (h) without modulator, (i) super resolution, (j) with modulator, (k) without modulator after bicubic interpolation, and (l) super resolution after bicubic interpolation. All results images are displayed on a logarithmic scale with a dynamic range of 40 dB.

### 3.2. Strands in an X-shaped arrangement

The same procedure was repeated for the second object configuration consisting of four hair strands in an X-shaped arrangement. The resulting images obtained at the depth corresponding to the surface of the object are presented in Fig. 6. The simulation object is shown in Fig. 6(a) and the corresponding experimental ground-truth object is presented in Fig. 6(g). The baseline reconstructions without the modulator are displayed in Fig. 6(b) for the simulation and Fig. 6(h) for the experiment. The reconstructed images obtained when the modulator was present are shown in Fig. 6(d) for the simulation and Fig. 6(j) for the experiment. The resulting super-resolution reconstructions are presented in Fig. 6(c) for the simulation and Fig. 6(i) for the experiment. To facilitate comparisons, the without-modulator and the super-resolution images after bicubic interpolation are shown in Fig. 6(e) and 6(f), respectively, for the simulation and in Fig. 6(k) and 6(l) for the experiment.



This preprint research paper has not been peer reviewed. Electronic copy available at: https://ssrn.com/abstract=5749641

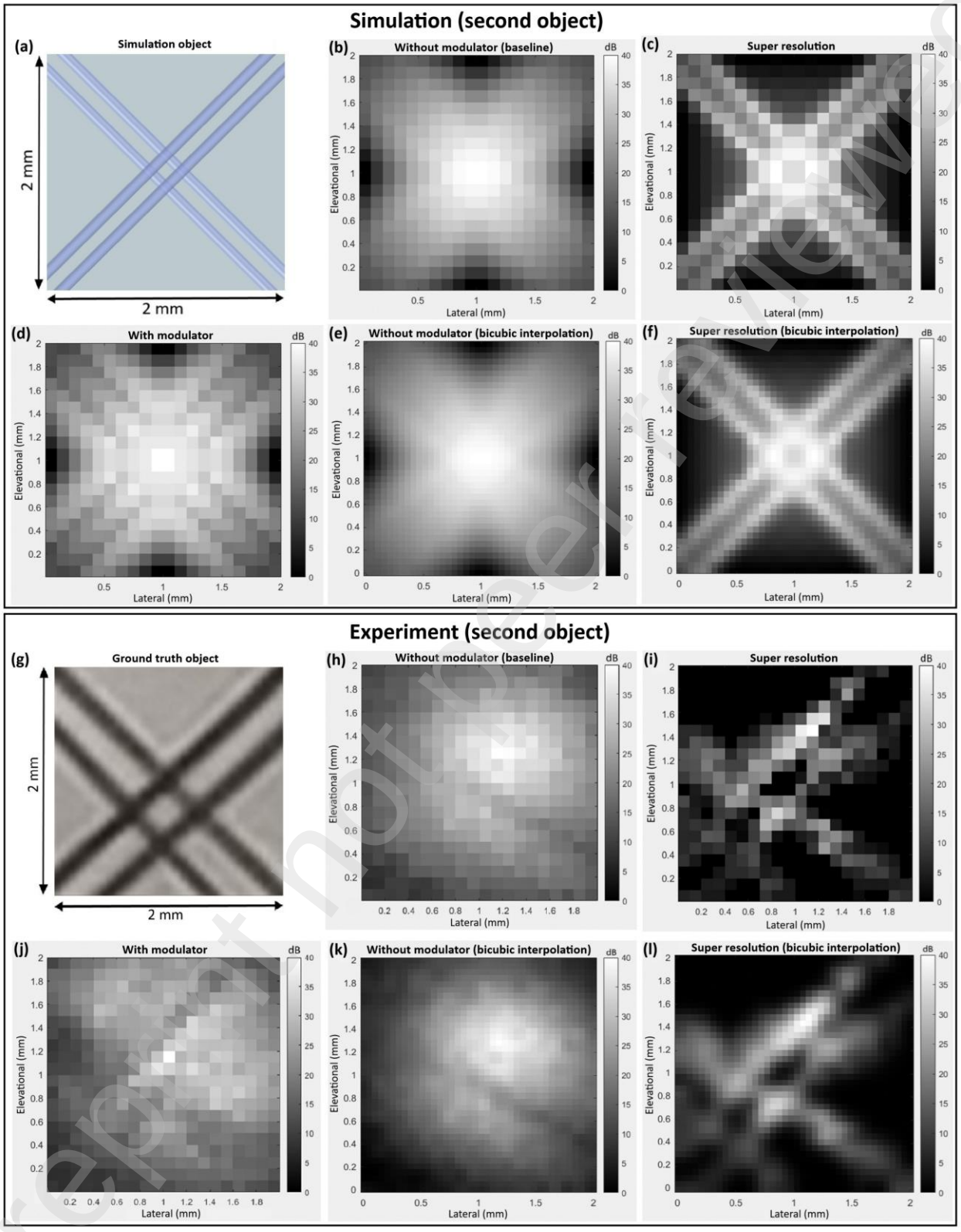


**Fig. 6** Reconstructed PA images at a fixed depth corresponding to the surface of the second object comprising four hair strands in an X-shaped arrangement. (a–f) Simulation: (a) simulation object, (b) without modulator (baseline), (c) super resolution, (d) with modulator, (e) without modulator after bicubic interpolation, and (f) super resolution



This preprint research paper has not been peer reviewed. Electronic copy available at: https://ssrn.com/abstract=5749641

after bicubic interpolation. (g–l) Experiment: (g) ground-truth experimental object, (h) without modulator (baseline), (i) super resolution, (j) with modulator, (k) without modulator after bicubic interpolation, and (l) super resolution after bicubic interpolation. All results images are displayed on a logarithmic scale with a dynamic range of 40 dB.

## 4. Discussion

The results presented in the figures are explained and discussed in detail in this section. Regarding the intermediate results of the multiphysics simulation of PA signal generation and propagation, Fig. 4(a) shows the initial ray distribution that represents the spatial energy deposition from the incident laser beam. The rays are directed toward the object from below to form a beam with a circular cross section. The symmetric ray pattern indicates a uniform Gaussian irradiation profile centered at the laser spot, characterized by maximum intensity at the center and a gradual decrease toward the edges, which is typical of many laser systems. The ray optics model accurately simulated the optical absorption pattern, which governs the resulting spatial distribution of the heating effect. The laser beam was collimated with minimal divergence, making it well suited for the shallow imaging depths that are commonly required in PA microscopy.

Fig. 4(b) shows the transient temperature rise in the *x*–*z* cross-sectional plane through the middle of the hair strands at 10 ns (one pulse width) after applying the laser pulse. The short pulse duration leads to rapid, localized heating via the photothermal effect, consistent with the thermal confinement conditions. The maximum temperature increase of approximately 0.7 °C occurred in the hair strands near the center of the laser spot, where the energy intensity was highest due to the Gaussian beam profile. This results in greater energy absorption compared with peripheral strands. In this study, black human hair strands were used as absorbers due to their high melanin content, which serves as a natural chromophore. Melanin strongly absorbs light in the visible and near-infrared ranges, making black hair an effective PA source. The temperature increase remained within biological tolerance limits, indicating safe and nondestructive energy deposition. The heat distribution was highly localized, with negligible lateral conduction over the 10-ns timescale.

Fig. 4(c) shows the mechanical displacement field in the same *x*–*z* cross-sectional plane resulting from thermoelastic expansion at 10 ns after applying the laser pulse. The displacements remained within the nanometer range (up to around 1 nm), indicating minute yet significant expansion due to localized heating. Its spatial distribution closely followed the temperature profile, confirming the direct coupling between thermal and mechanical responses in the PA effect. The outward symmetry of the displacement field reflected isotropic expansion, consistent with uniform material properties and isotropic elastic behavior assumed for the medium. Fig. 4(d) presents the pressure distribution generated by the rapid thermoelastic expansion of the heated regions. This pressure serves as the primary PA source, governed by the Grüneisen parameter and the local temperature profile. The peak pressures reached approximately 1.7 MPa, which are typical for strongly absorbing chromophores under nanosecond-pulse excitation. The circular symmetry and sharp confinement of the pressure sources further confirmed the thermal and stress confinement conditions that are essential for efficient PA signal generation.

The pressure distribution obtained was inputted as the initial condition in the acoustic pressure physics in the last step. Fig. 4(e) shows the propagation of the PA wave in the same *x*–*z* cross-sectional plane at 12 μs after its generation, which illustrates the acoustic pressure field that evolved in the simulation domain. At that time point the pressure reached approximately 7.5 kPa. The acoustic wave propagated upward and eventually reached the transducer positioned at the top, where it was detected to produce the signals required for subsequent image reconstruction.



Preprint not peer reviewed

This preprint research paper has not been peer reviewed. Electronic copy available at: https://ssrn.com/abstract=5749641

Fig. 5 presents the results of the reconstructed PA images in the elevational–lateral plane at a specific depth for the first object consisting of three parallel hair strands. The object configurations considered for inclusion in the simulation and experiment are shown in Fig. 5(a) and 5(g), respectively, to facilitate comparisons with the reconstructed PA images. As mentioned above, based on the specifications of our transducer, the theoretical diffraction-limited lateral resolution without PSF modulation was around 0.6 mm. This is consistent with the results shown in Fig. 5(b) and 5(h), where the hair strands separated by 0.1–0.2 mm were not resolvable in either the simulation or experiment due to the lateral resolution being inadequate. The reconstructed with-modulator images in Fig. 5(d) and 5(j) show decreased signal intensities at the hair strand positions. This is expected due to the modulator blocking the PA signals emitted directly from the hair strands located underneath it. In contrast, the regions without hair strands show little to no changes in signal amplitude, since the signals detected in those areas predominantly originated from nearby regions that were not directly blocked by the modulator.

The super-resolution images produced after the signal processing step involving the subtraction of the modulated and unmodulated signals are shown in Fig. 5(c) and 5(i) for the simulation and experiment, respectively. These images clearly demonstrate improved spatial resolution, since all three hair strands became distinguishable, even those separated by as little as 0.1 mm. According to the PSF modulation theory, the resolution improvement is governed by the size of the modulator [17]. The spatial resolution is improved because the modulator selectively attenuates a portion of the PSF corresponding to its own size, enabling finer spatial features to be resolved through the application of differential signal processing. We found that the conventional diffraction-limited lateral resolution of approximately 0.6 mm was effectively improved to around 0.1 mm, which corresponds to the minimum distinguishable distance between the two closely spaced hair strands. This represents an approximately sixfold improvement, enabling features separated by only 0.1 mm to be clearly distinguished.

It should also be noted that while both the simulation and experimental results in Fig. 5 show clear resolution improvement, the simulation results appear smoother. The experimental images exhibit asymmetries and noise due to practical factors such as misalignment and coupling variations. Despite these differences, all three hair strands were successfully resolved in both the simulation and experimental results, confirming the effectiveness of the approach.

To facilitate comparisons and better illustrate the effects of PSF modulation on the reconstructed PA images, bicubic interpolation was applied to both the without-modulator images [Fig. 5(e) and 5(k) for the simulation and experiment, respectively] and the super-resolution images [Fig. 5(f) and 5(l), respectively] to suppress raster-related pixelation. This interpolation method improves visual quality by producing smoother intensity transitions between pixels, which reveals finer structural details without introducing artifacts. Overall, the interpolated images in Fig. 5 further validate the effectiveness and generalizability of the PSF modulation approach for achieving super-resolution PAI. The consistent recovery of fine spatial features—along with the sixfold improvement in lateral resolution—demonstrates the robustness of this method and its ability to overcome the diffraction limit, highlighting its broad applicability to high-resolution PAI.

To further validate the efficacy of the PSF modulation approach in resolving more-complex and closely spaced features, we applied the same methodology to objects in an X-shaped arrangement, as shown in Fig. 6. This arrangement represents a more-challenging scenario due to the presence of intersecting structures with small spatial separations. In the baseline images without modulation [Fig. 6(b) and 6(h), and Fig. 6(e) and 6(k) after bicubic interpolation], both the simulation and experimental results show a blurred central region where the intersecting strands are indistinguishable due to the system's diffraction-limited



This preprint research paper has not been peer reviewed. Electronic copy available at: https://ssrn.com/abstract=5749641

resolution. After introducing the modulator [Fig. 6(d) and 6(j)], signal attenuation is again observed at the locations of the object, confirming that the modulator selectively blocked part of the PSF associated with the target structures. The experimental image shows greater variability and noise, but the overall attenuation trend remains consistent with that for the simulation.

Following differential signal processing, the super-resolution images [Fig. 6(c) and 6(i), and Fig. 6(f) and 6(l) after bicubic interpolation] reveal the full X-shaped arrangement with significantly improved clarity. The crossing lines are sharply resolved in the simulation images, demonstrating symmetric and well-defined features. Some background noise persists in the experimental images, but the intersecting strands became clearly distinguishable, further confirming the improvement in resolution.

These results are consistent with the findings for the object comprising three parallel hairs, supporting that the achieved improvement in resolution is a general outcome of the PSF modulation principle rather than being restricted to a specific type of object. The observed resolution improvement again approached the scale of the modulator size (0.1 mm), representing a sixfold increase over the conventional diffraction-limited resolution of ~0.6 mm, and confirming the method's robustness in resolving features markedly smaller than the diffraction limit even in geometrically complex configurations.

One of the primary limitations of this approach in real biomedical imaging applications is the practical difficulty of placing a physical modulator within tissue at various depths—the ability to effectively modulate the PSF across the entire imaging domain requires the modulator to be accurately positioned not only laterally but also axially, aligning precisely with the transducer's focal point at different depths. Therefore, the fundamental challenge of this method is minimizing the object–modulator distance in order to ensure effective modulation. Inserting and controlling such a modulator inside biological tissue poses significant challenges related to anatomical constraints, tissue heterogeneity, and invasiveness. These factors restrict the applicability of fixed physical modulators for in-vivo application, especially in deep or volumetric imaging situations. This limitation could be addressed by using other types of modulators, as explained below.

In the context of PSF modulation, the modulator can be any device that locally perturbs the system's PSF to suppress signal contributions from the central region of the acoustic or optical response. This can be achieved either by blocking the acoustic waves generated in PAI (acoustical modulation) or by obstructing light delivery at a very small spatial location (optical modulation), with either approach effectively attenuating the core of the PSF and thereby acting as an amplitude modulator. Phase modulation using focused shear waves can also be performed by inducing localized phase shifts in the imaging wave. Both situations will alter the PSF, and the resulting spatial asymmetry in the PSF enables the recovery of high-frequency components via differential signal processing, thereby achieving super-resolution. While the present study focused on a fixed physical amplitude modulator, future implementations of PSF modulation could employ more-flexible, programmable, and noninvasive approaches, especially for in-vivo and deep-tissue imaging applications. Several strategies that can extend the applicability of PSF modulation in biological imaging are discussed below.

### 4.1. Phase modulators

Shear waves acting as phase modulators can be generated remotely at the focal point of a transducer at different depths inside tissue using the acoustic radiation force (ARF), which enables PSF modulation at arbitrary depths through external acoustic excitation applied outside the tissue. A recent conference paper described the development and analysis of a method for super-resolution imaging based on remotely generated modulators using focused shear waves [28]. That study demonstrated that these shear waves—



Preprint not peer reviewed

This preprint research paper has not been peer reviewed. Electronic copy available at: https://ssrn.com/abstract=5749641

created by ARFs from focused Bessel or cosine beams—can modulate the PSF of US and PAI systems to overcome the diffraction limit. The author used theoretical modeling and computer simulations to show how to reduce side lobes and improve the SNR via resonance and coherent interference [28]. This approach enabled high-resolution imaging of soft biological tissues deep within the body; however, further experimental validation of the approach is required.

### 4.2. External amplitude modulators

External acoustical or optical amplitude modulators can be placed on the surface of the object (without penetration) for performing shallow-tissue acoustic-resolution PA microscopy (AR-PAM) at imaging depths up to ~0.4 mm, such as in-vivo imaging of the epidermis and papillary dermis, as well as in-vitro microscopy. This approach achieves resolutions comparable to those of optical-resolution PA microscopy (OR-PAM). AR-PAM using external modulators offers a relatively compact, flexible, easily integrated, and implementation-friendly alternative to OR-PAM in these cases [17].

### 4.3. Internal amplitude modulators

Using internal amplitude modulators for depth targeting can extend the applicability of this technique to deeper in-vivo imaging, where external (i.e., surface-based) modulation is no longer effective. Some of the feasible methods are as follows:

- **Focused US with nanoparticles:** Low-boiling-point nanoparticles such as perfluorocarbon droplets can be vaporized using high-frequency focused US at 40–50 MHz, which generates transient cavities that act as localized modulators at depth [17]. This strategy provides depth selectivity for PSF modulation. However, several challenges need to be addressed, including precisely controlling the size and location of the cavities (which directly define the effective modulator size and the lateral resolution achievable), avoiding cavity instability and tissue heating, and overcoming the strong attenuation of high-frequency US in tissue that reduces the penetration depth.
- **Magnetic nanoparticles:** Superparamagnetic nanoparticles, such as iron oxide, can be guided and accumulated by an external magnetic field to act as controllable modulators, enabling localized in-depth PSF modulation [17]. However, achieving spatial confinement on the submillimeter scale (which determines the effective modulator size) requires strong and precisely controlled magnetic field gradients, which is technically demanding and may pose challenges for in-vivo applications.
- **Other triggerable agents:** The internal amplitude modulation concept can also be extended to both acoustical and optical modulators. For example, optically triggered bubbles or light-absorbing agents can serve as transient modulators that are activated in specific regions for localized modulation of the PSF [17]. However, achieving precise spatial confinement at depth remains a major challenge, and localized heating or photothermal damage may further restrict their safety for in-vivo application.

Future research could further explore these potential strategies and systematically evaluate their feasibility, safety, and effectiveness in practical imaging applications. This novel PSF modulation technique is still in a preliminary stage, and additional studies are required before it can be implemented clinically. The present work marks an important first step in demonstrating the potential, feasibility, and effectiveness of PSF modulation for achieving super-resolution PAI, and it may serve as a foundation for future studies and further refinements of the technique.



Preprint not peer reviewed

This preprint research paper has not been peer reviewed. Electronic copy available at: https://ssrn.com/abstract=5749641

## 5. Conclusion

This study has introduced and experimentally demonstrated a novel super-resolution PAI technique based on PSF modulation. Our implementation of PSF amplitude modulation using a localized physical modulator as well as differential signal processing could successfully improve the spatial resolution of PAI beyond the conventional acoustic diffraction limit. Comprehensive FEM simulations along with controlled experiments using two object configurations—three parallel strands and four strands in an X-shaped arrangement—validated the proposed approach. The reconstructed images showed that features separated by as little as 0.1 mm could be clearly resolved, which represents a sixfold improvement in lateral resolution over the original system resolution of approximately 0.6 mm.

These results establish a strong proof of concept for utilizing PSF modulation in PAI, a strategy that has not previously been explored in this application. The method provides a generalizable framework for improving the spatial resolution beyond the acoustic diffraction limit without relying on improved transducer characteristics or motion-dependent techniques. The successful reconstruction of two object geometries in both simulations and experiments has highlighted the versatility and applicability of the approach. Moreover, the method demonstrated consistent performance under experimental conditions, demonstrating resilience to alignment variations and background noise, which underscores its practical feasibility.

While the current implementation used a fixed physical modulator, which presents limitations for in-vivo and deep imaging, this study has laid the foundation for future advancements. These could involve the development of noninvasive modulators, such as those mentioned in the Discussion section, as well as integration with advanced signal processing methods or deep learning. Such extensions could enable real-time, high-resolution PAI in dynamic and clinically relevant environments, broadening the impact of this method across biomedical and diagnostic imaging applications.

## Acknowledgments

This work was financially supported by the Center for Advanced Computing and Imaging in Biomedicine (NTU-114L9007), part of the Featured Areas Research Center Program within the framework of the Higher Education Sprout Project, funded by the Ministry of Education (MOE) in Taiwan.

## References

1. Wang, L.V. and S. Hu, *Photoacoustic tomography: in vivo imaging from organelles to organs.* Science, 2012. **335**(6075): p. 1458–1462.
2. Ntziachristos, V., *Going deeper than microscopy: the optical imaging frontier in biology.* Nature Methods, 2010. **7**(8): p. 603–614.
3. Xu, M. and L.V. Wang, *Photoacoustic imaging in biomedicine.* Review of Scientific Instruments, 2006. **77**(4): p. 041101.
4. Shi, J., Y. Tang, and J. Yao, *Advances in super-resolution photoacoustic imaging.* Quantitative Imaging in Medicine and Surgery, 2018. **8**(8): p. 724–732.
5. Luís Dean-Ben, X. and D. Razansky, *Localization optoacoustic tomography.* Light: Science & Applications, 2018. **7**(4): p. 18004.
6. Kim, J., et al., *Super-resolution localization photoacoustic microscopy using intrinsic red blood cells as contrast absorbers.* Light: Science & Applications, 2019. **8**(1): p. 103.
7. Nie, L. and X. Chen, *Structural and functional photoacoustic molecular tomography aided by emerging contrast agents.* Chemical Society Reviews, 2014. **43**(20): p. 7132–7170.



Preprint not peer reviewed

This preprint research paper has not been peer reviewed. Electronic copy available at: https://ssrn.com/abstract=5749641

8. Basak, S., et al., *Super-resolution optical fluctuation imaging.* Nature Photonics, 2025. **19**: p. 229–237.
9. Chen, Z., et al., *Multifocal structured illumination optoacoustic microscopy.* Light: Science & Applications, 2020. **9**(1): p. 152.
10. Murray, T.W., et al., *Super-resolution photoacoustic microscopy using blind structured illumination.* Optica, 2016. **4**(1): p. 17–22.
11. Yu, Z., H. Li, and P. Lai, *Wavefront shaping and its application to enhance photoacoustic imaging.* Applied Sciences, 2017. **7**(12): p. 1320.
12. Xia, F., et al., *Optical wavefront shaping in deep tissue using photoacoustic feedback.* Journal of Physics: Photonics, 2024. **6**(4): p. 043005.
13. Manwar, R., M. Zafar, and Q. Xu, *Signal and image processing in biomedical photoacoustic imaging: a review.* Optics, 2020. **2**(1): p. 1–24.
14. Park, S., et al., *Adaptive beamforming for photoacoustic imaging.* Optics Letters, 2008. **33**(12): p. 1291–1293.
15. Shechtman, Y., *Recent advances in point spread function engineering and related computational microscopy approaches: from one viewpoint.* Biophysical Reviews, 2020. **12**(6): p. 1303–1309.
16. Lu, J.-y., *Super-resolution imaging with modulation of point spread function.* The Journal of the Acoustical Society of America, 2023. **153**(3_Supplement): p. A28.
17. Lu, J.-y., *Modulation of point spread function for super-resolution imaging.* IEEE Transactions on Ultrasonics, Ferroelectrics, and Frequency Control, 2024. **71**(1): p. 153–171.
18. Lu, J.-y., *Remote super-resolution mapping of wave fields.* IEEE Transactions on Ultrasonics, Ferroelectrics, and Frequency Control, 2025. **72**(3): p. 370–379.
19. Soltani, M., R. Rahpeima, and F.M. Kashkooli, *Breast cancer diagnosis with a microwave thermoacoustic imaging technique—a numerical approach.* Medical & Biological Engineering & Computing, 2019. **57**: p. 1497–1513.
20. Rahpeima, R., C.-H. Wen, and P.-C. Li, *A computationally efficient FEM platform for comprehensive simulations of photoacoustic imaging.* Computer Methods and Programs in Biomedicine, 2025. **261**: p. 108620.
21. Rahpeima, R., M. Soltani, and F.M. Kashkooli, *Numerical study of microwave induced thermoacoustic imaging for initial detection of cancer of breast on anatomically realistic breast phantom.* Computer Methods and Programs in Biomedicine, 2020. **196**: p. 105606.
22. Rahpeima, R. and C.-A. Lin, *A comprehensive numerical procedure for high-intensity focused ultrasound ablation of breast tumour on an anatomically realistic breast phantom.* PloS One, 2024. **19**(10): p. e0310899.
23. Rahpeima, R. and C.-A. Lin, *Numerical study of magnetic hyperthermia ablation of breast tumor on an anatomically realistic breast phantom.* PloS One, 2022. **17**(9): p. e0274801.
24. Rahpeima, R. and R. Ebrahimi, *A numerical approach for optimization of the working fluid of a standing-wave thermo-acoustic refrigerator.* Engineering with Computers, 2023. **39**(4): p. 2717–2733.
25. Rahpeima, R. and R. Ebrahimi, *Numerical investigation of the effect of stack geometrical parameters and thermo-physical properties on performance of a standing wave thermoacoustic refrigerator.* Applied Thermal Engineering, 2019. **149**: p. 1203–1214.
26. Lu, J.-y., *Reconstruction methods for super-resolution imaging with PSF modulation.* The Journal of the Acoustical Society of America, 2024. **155**(3_Supplement): p. A54.
27. Beard, P., *Biomedical photoacoustic imaging.* Interface Focus, 2011. **1**(4): p. 602–631.
28. Lu, J.-y., *Generation of modulators for super-resolution imaging.* The Journal of the Acoustical Society of America, 2025. **157**(4_Supplement): p. A54.



Preprint not peer reviewed

This preprint research paper has not been peer reviewed. Electronic copy available at: https://ssrn.com/abstract=5749641

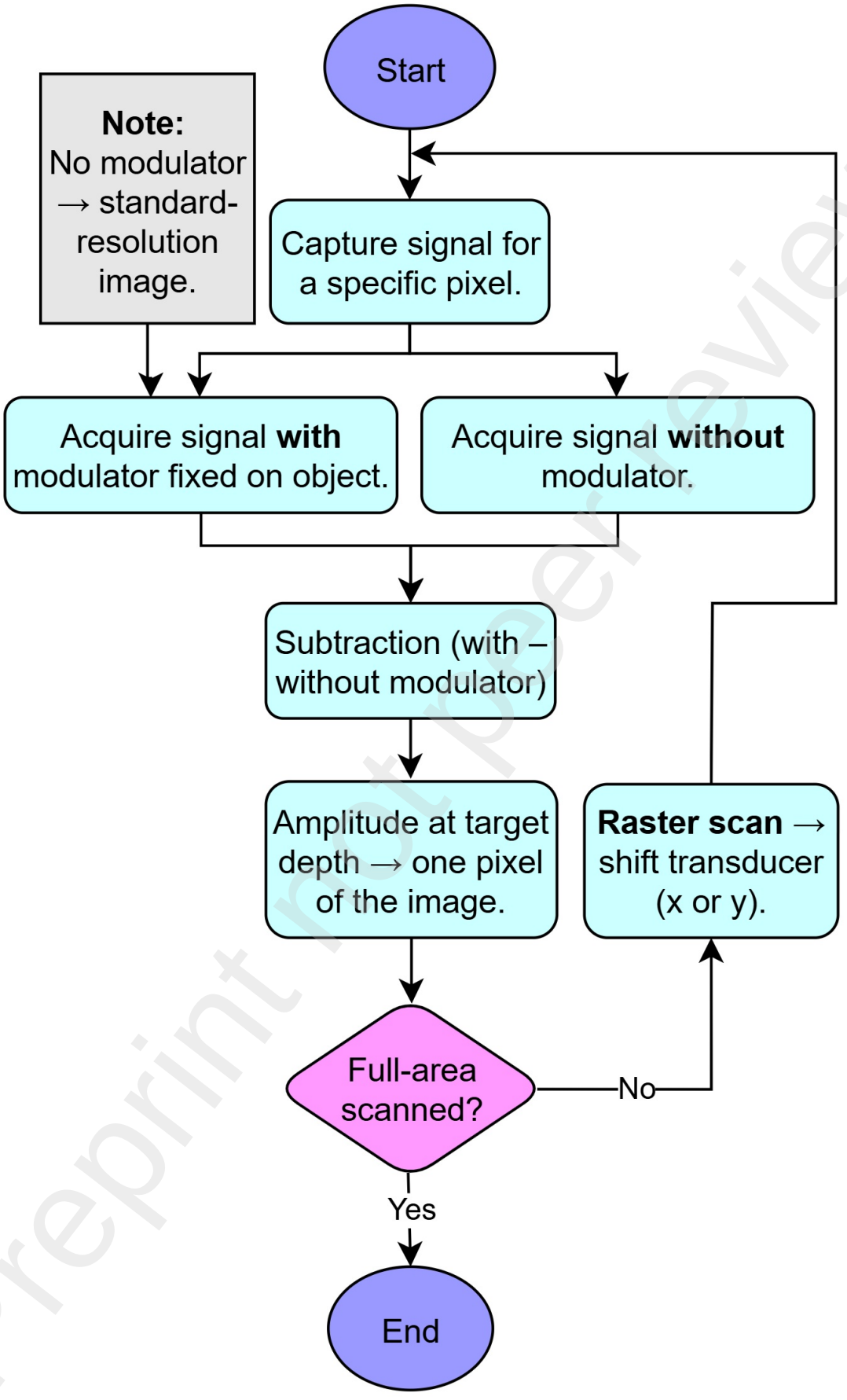


Preprint not peer reviewed

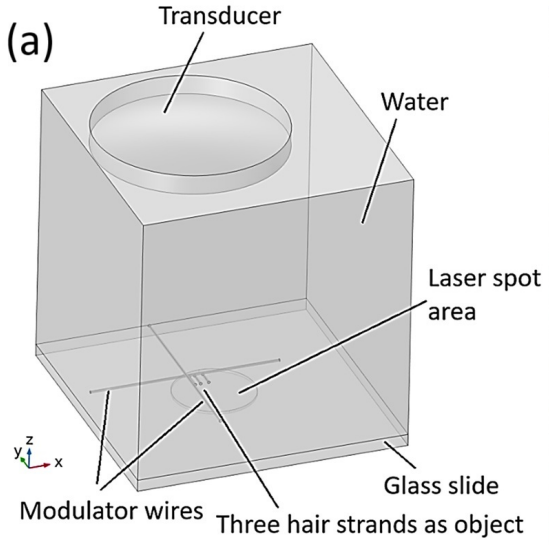


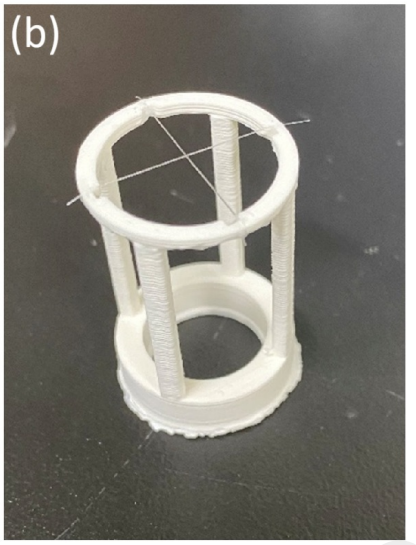


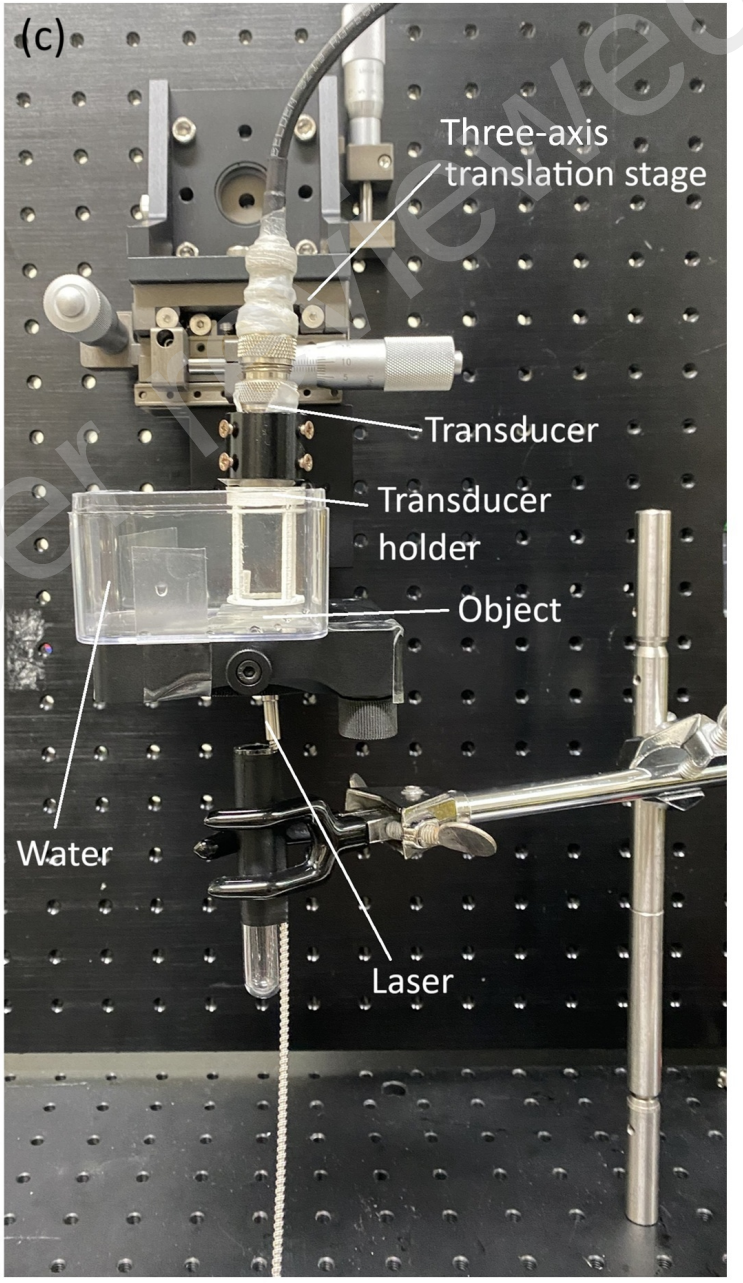


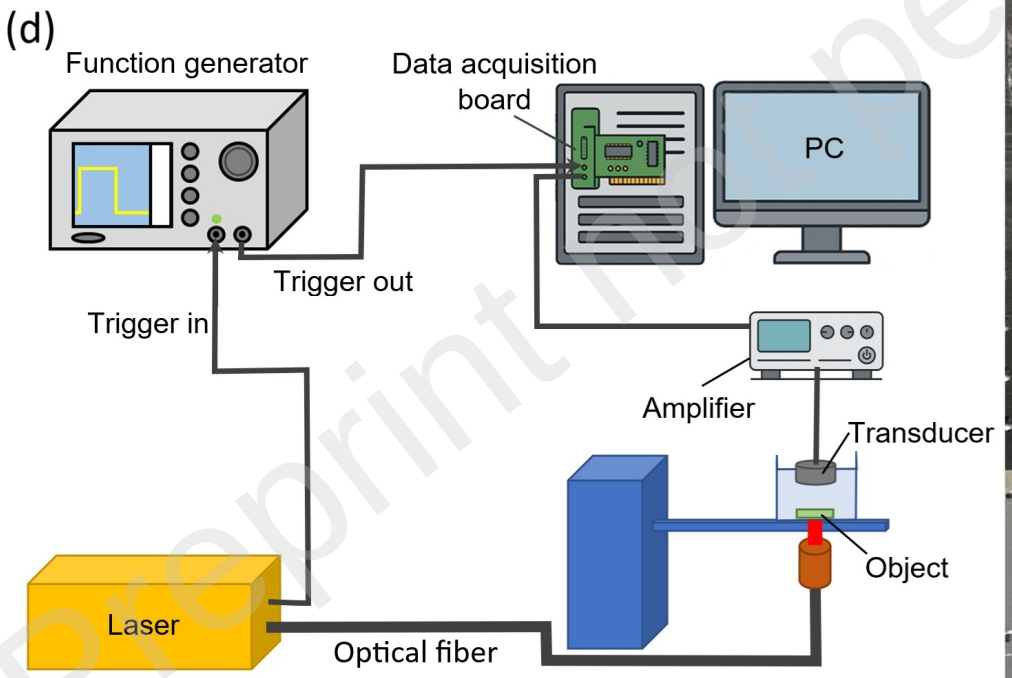


Preprint not peer reviewed

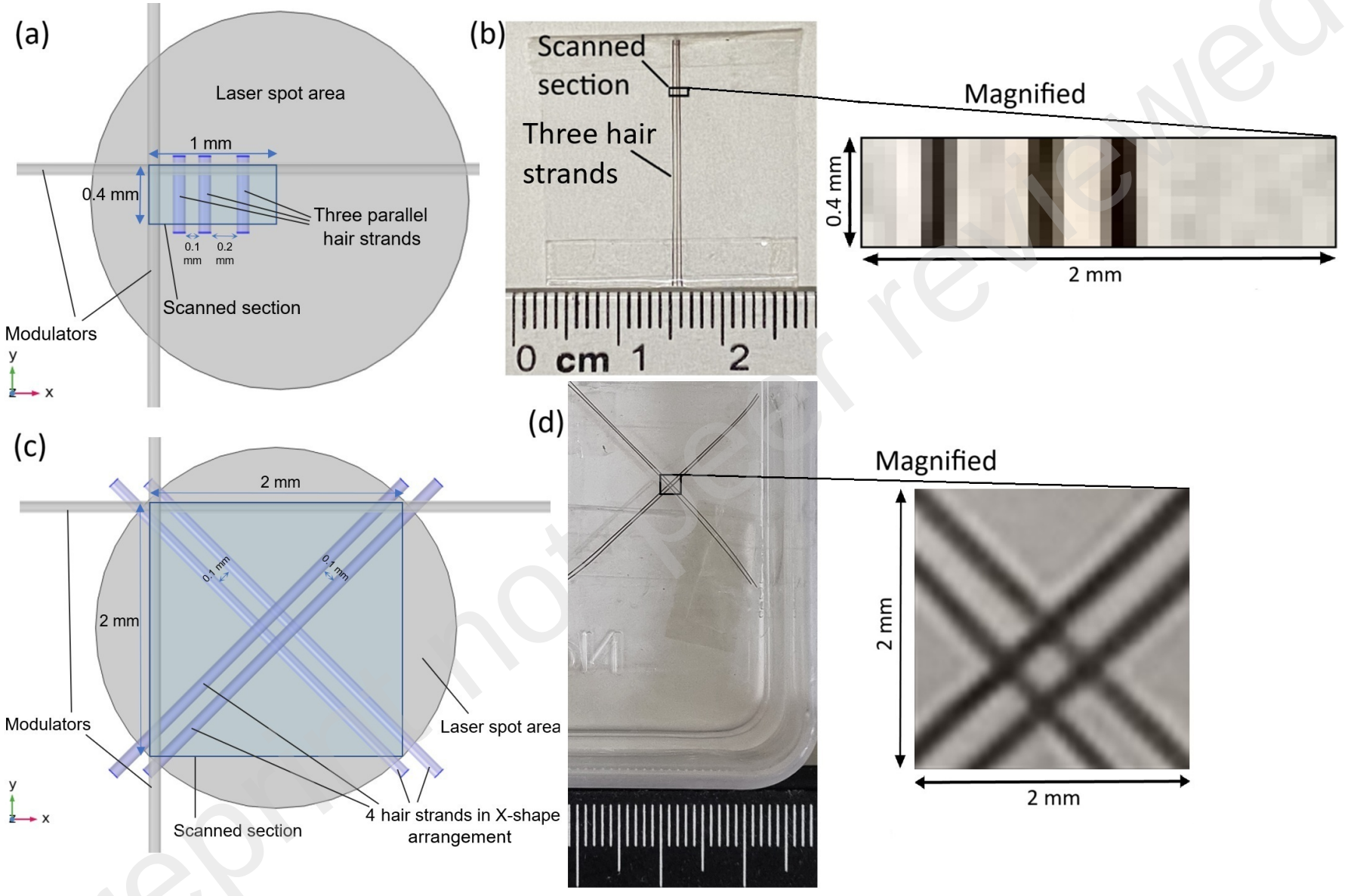


Preprint not peer reviewed

(a) Initial ray configuration at the laser spot area

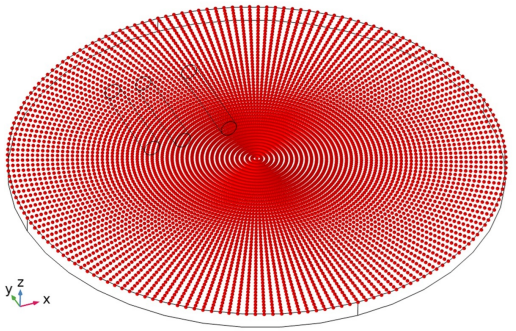

(b) Temperature difference after 10 ns (°C)

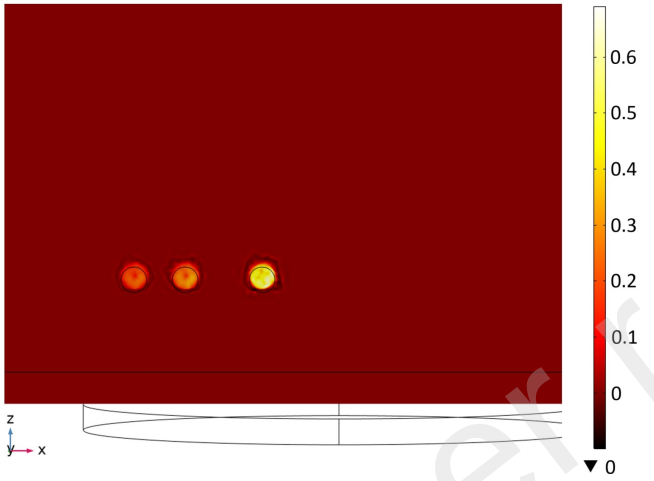


(c) Displacement magnitude after 10 ns (mm)

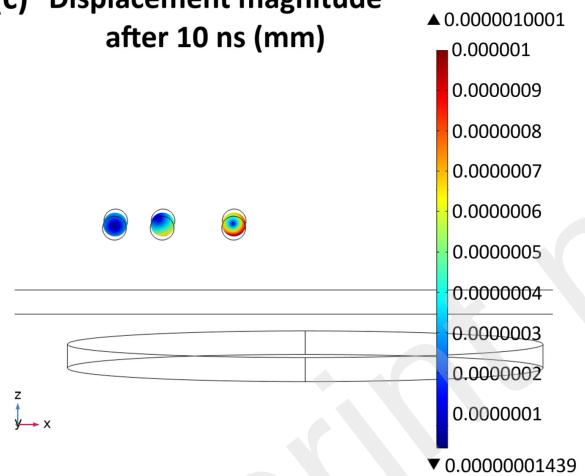


(d) Pressure after 10 ns (N/m$^2$)

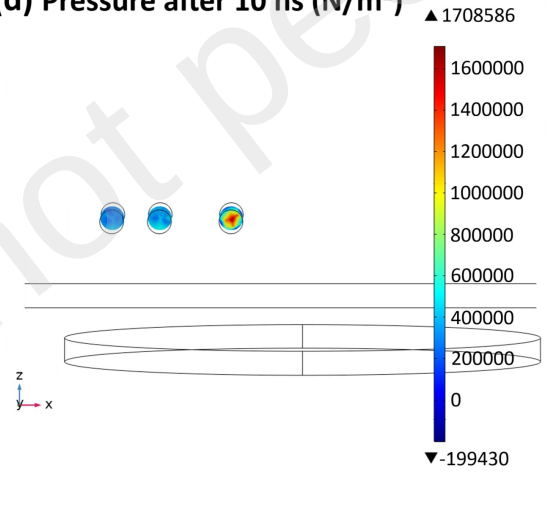


(e) Acoustic pressure (Pa)

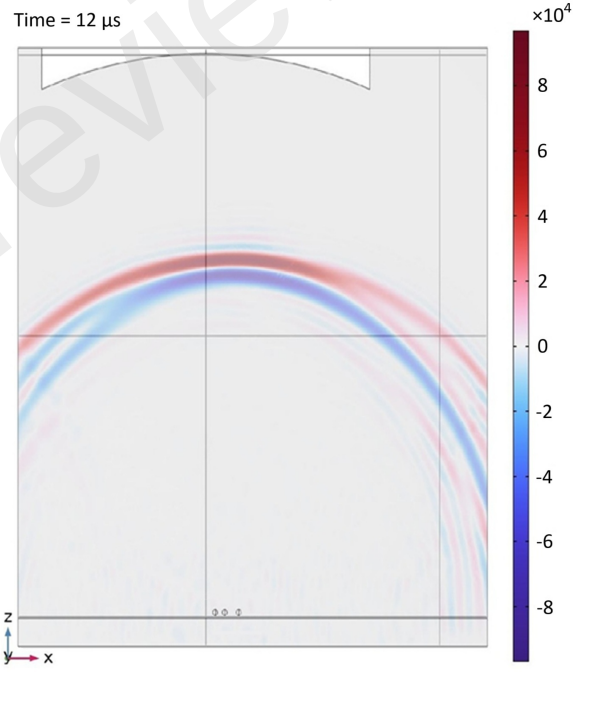


Preprint not peer reviewed

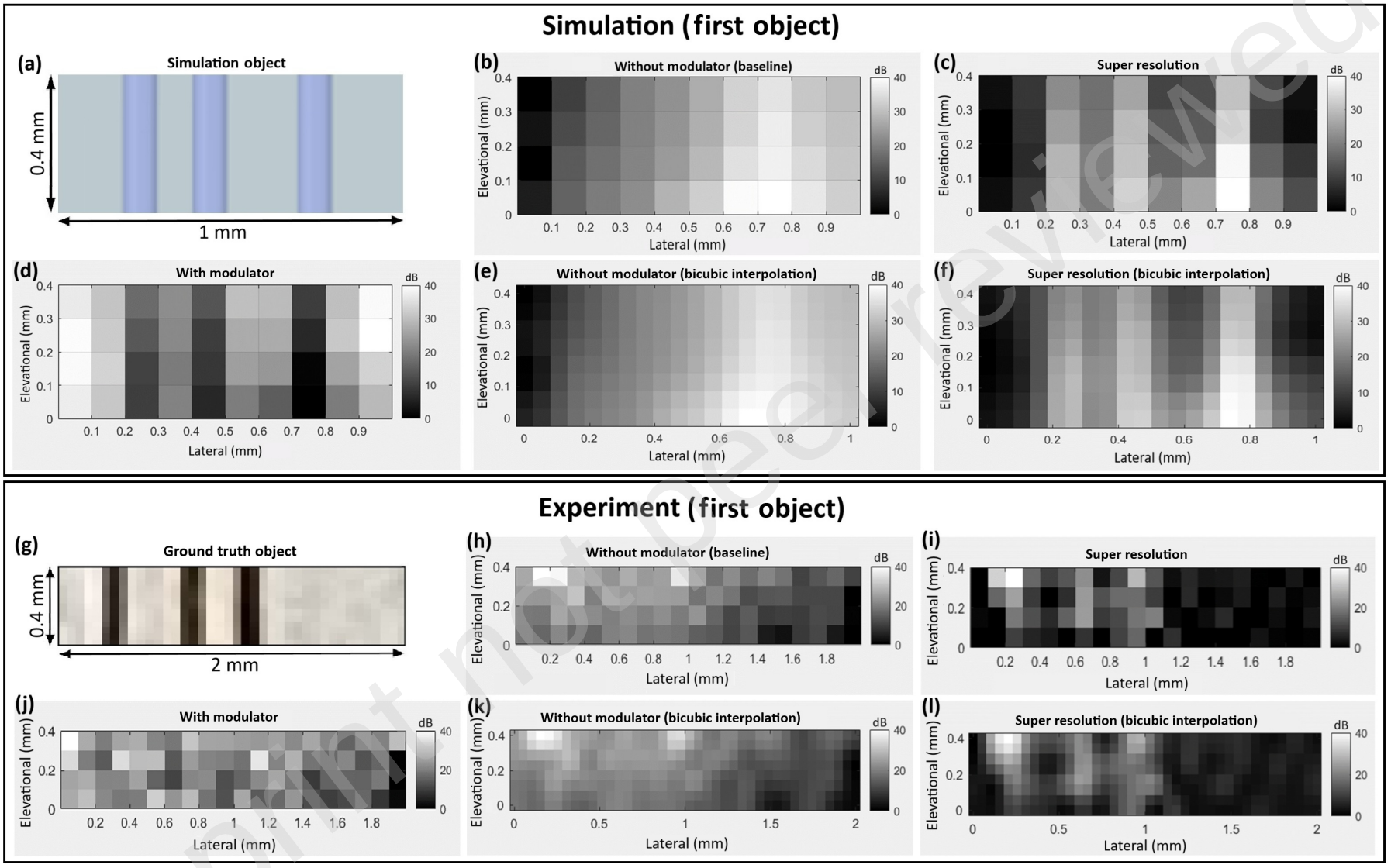


Preprint not peer reviewed

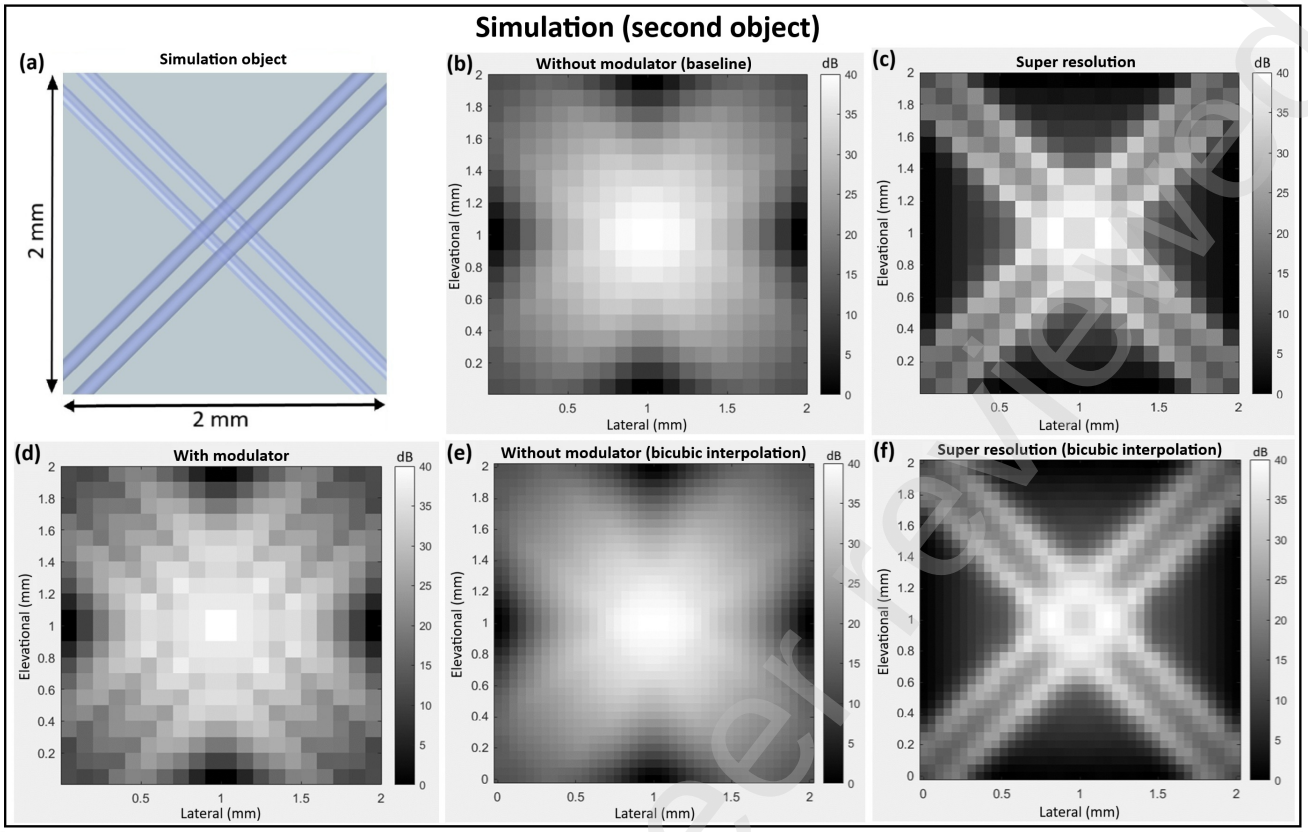


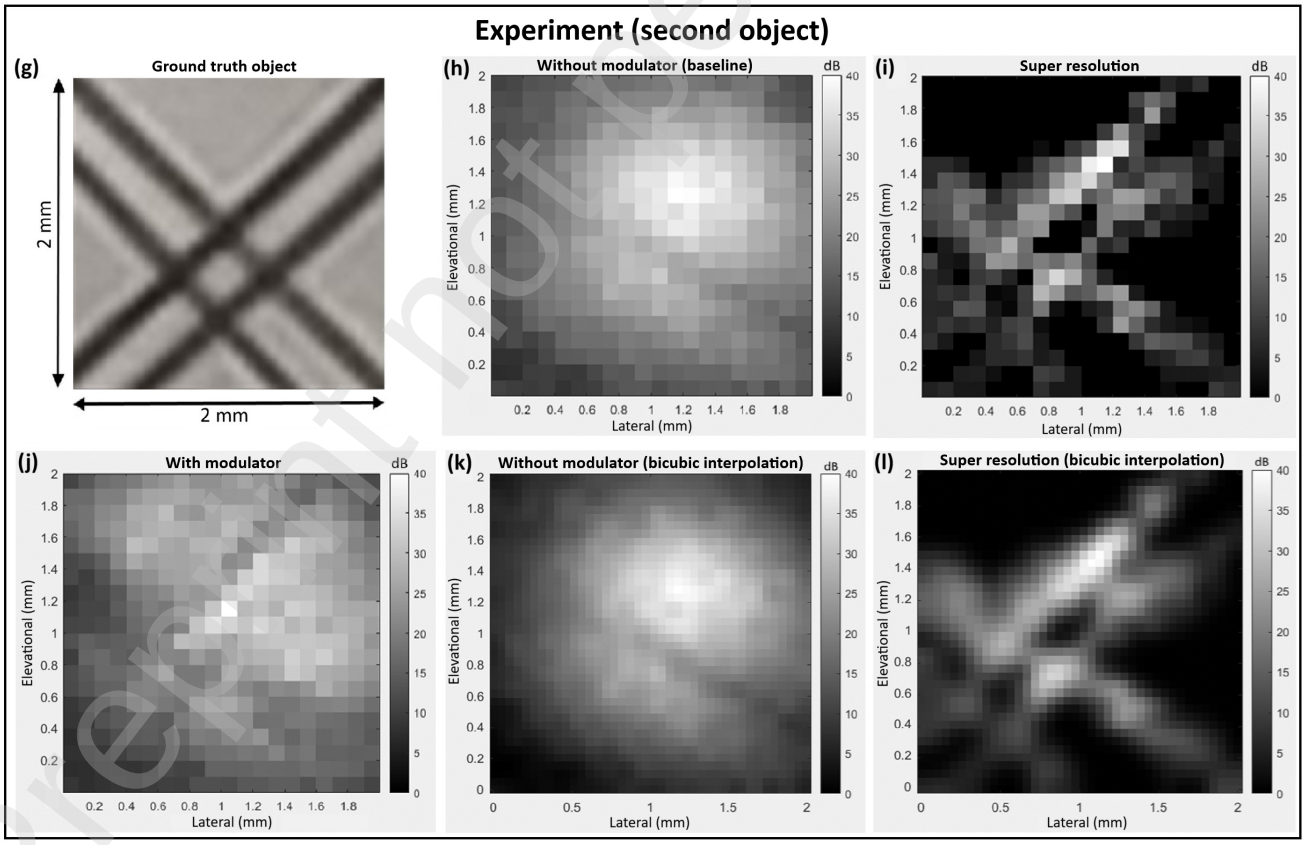


Preprint not peer reviewed